5

Electron Holography of Magnetic Nanostructures

M.R. McCartney, R.E. Dunin-Borkowski, and D.J. Smith

Electron holography is an electron microscope imaging technique that permits quantitative measurement of magnetic fields with spatial resolution approaching the nanometer scale. The theoretical background and usual experimental setup for electron holography are first briefly described. Applications of the technique to magnetic materials and nanostructures are then discussed in more detail. Future prospects are summarized.

5.1 Introduction

The transmission electron microscope (TEM) is an essential tool that is in widespread use for microstructural characterization. Although there are many different TEM imaging modes, most cannot be used to characterize magnetic fields within or surrounding a sample because they are insensitive to changes in the phase of the electron beam. Lorentz microscopy, as described in Chap. 4, uses defocused imaging to distinguish magnetic features such as domain walls [1, 2]. In this approach, which has several closely related variants [3], high-energy electrons of the incident beam are deflected sideways by the magnetic field of the sample to produce bands of light and dark contrast that correspond to local changes in the magnetic field strength or orientation. Compared with electron holography, these Lorentz imaging modes have the advantages that real-time observation of changing domains is possible and no vacuum reference wave is required. However, longer-range magnetic fields are not easily mapped, and compositional contributions to the contrast from the edges of nanostructured elements may be significant, so that magnetic nanostructures become more difficult to characterize as their dimensions are reduced.

Electron holography offers an alternative and powerful approach for characterizing magnetic microstructure. In this technique, access to both the phase and the amplitude of the electron wave can be obtained after the electrons have traveled through the sample [4, 5]. Since the phase change of the electron wave can be related directly to the magnetic (and electric) fields in the sample, magnetic materials can be studied at high spatial resolution and sensitivity using electron holography. The

technique is intrinsically capable of achieving a spatial resolution of better than 1 nm for magnetic materials, but this resolution level has yet to be demonstrated on real samples, due primarily to practical limitations. These limitations are associated with the recording process and/or the subsequent hologram processing, with the available signal-to-noise ratio in the hologram being a major restriction. Moreover, because the electrons are transmitted through the specimen, the sample thickness for electron holography is limited to about 500 nm to avoid degradation of the hologram due to multiple scattering effects. One particular attraction of electron holography relative to most other magnetic imaging techniques, which measure the first or second differential of the phase, is that much smaller sample regions are accessible for analysis because unwanted effects arising from local variations in composition and sample thickness can be removed more easily. With the ongoing downscaling of dimensions for magnetic storage devices, holographic approaches thus offer much potential for solving important industrial problems, as well as contributing toward the advancement of fundamental scientific knowledge.

The technique of electron holography is based on the interference of two (or more) coherent electron waves to produce an interferogram or "hologram." This interference pattern must then be processed in order to retrieve, or reconstruct, the complex electron wavefunction, which carries the desired phase and amplitude information about the sample. At least 20 different forms of electron holography have been identified [6], many of which have been demonstrated in practice. Off-axis (or sideband) electron holography, as illustrated in Fig. 5.1, is the mode most commonly used. In this approach, the electrostatic biprism, as developed originally by Möllenstedt and Düker [7], is used to overlap the electron wave scattered by the sample with a vacuum reference (Fig. 5.1).

The earliest attempts at electron holography [8] were severely restricted because the tungsten hairpin filament used as their electron source had limited brightness, in turn limiting the available coherence of the incident beam. The development of the high-brightness, field-emission electron gun (FEG) for the TEM [9] made possible the practical implementation of electron holography. All electron holography applications subsequently reported in the scientific literature have used an FEG as the electron source.

Off-line optical methods have traditionally been used to achieve wavefunction reconstruction from electron holograms [10], but digital processing of electron holograms has become widespread in recent years [11] due to the advent of the slow-scan charge-coupled-device (CCD) camera for digital recording [12]. Coupled with the recent rapid growth in computer speed and memory, quantitative digital electron holography has become a reality [13, 14]. Digital recording with the CCD camera also provides linear output over a large dynamic range, so that correction for nonlinearity of photographic-plate optical density is no longer needed. The speed, accuracy, and reliability of the reconstruction process are greatly enhanced, and accurate registration of sample and reference holograms is easily achieved (see below).

In this chapter, we first outline the basic principles of electron holography, from both theoretical and practical points of view. We briefly describe some of the more general applications of the technique, in particular to magnetic materials such as

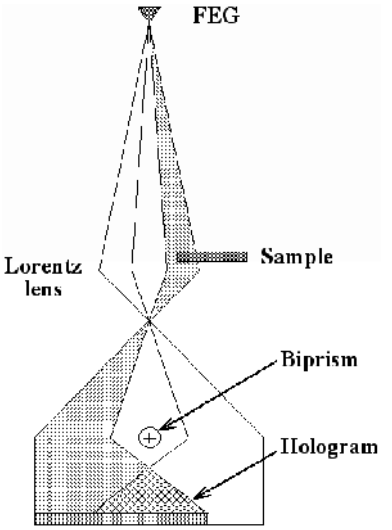

Fig. 5.1. Schematic ray diagram showing setup used for off-axis electron holography in the TEM. Essential components are the field emission electron source (FEG) used to provide coherent illumination and the electrostatic biprism, which causes overlap of object and (vacuum) reference waves

recording media and hard magnets. Results for magnetic nanostructures are then presented in more detail. Finally, possible opportunities for future developments are discussed. These include the in situ application of variable external fields and real-time viewing of dynamic events.

5.2 Basis of Electron Holography

5.2.1 Theoretical Background

The electron wave incident on a TEM sample undergoes phase shifts due to the mean inner potential (i.e., the composition and density) of the sample, as well as the in-plane component of the magnetic field integrated along the incident beam direction. Neglecting dynamical diffraction, which can have a significant effect on crystalline materials oriented close to major zone axes [15], the electron phase change after passing through the sample, relative to a wave that has passed only through vacuum, is given (in one dimension) by the expression

$$\phi(x) = C_E \int V(x, z)\,\mathrm{d}z - \frac{\mathrm{e}}{\hbar} \iint B_\perp(x, z)\,\mathrm{d}x\,\mathrm{d}z\,, \tag{5.1}$$

where z is the incident beam direction, x is a direction in the plane of the sample, V is the mean inner potential, and $\mathbf{B}$ is the component of the magnetic induction perpendicular to both x and z. The constant C_E is given by the expression

$$C_E = \frac{2\pi}{\lambda E}\frac{E + E_0}{E + 2E_0}\,, \tag{5.2}$$

where λ is the wavelength, and E and E_0 are the kinetic and rest mass energies, respectively, of the incident electron.

When neither V nor B vary with z within the sample thickness t, and neglecting any electric and magnetic fringing fields outside the sample, this expression can be simplified to

$$\phi(x) = C_E V(x)t(x) - \frac{\mathrm{e}}{\hbar}\int B_\perp(x)t(x)\,\mathrm{d}x\,. \tag{5.3}$$

Differentiation with respect to x leads to

$$\frac{\mathrm{d}\phi(x)}{\mathrm{d}x} = C_E\frac{\mathrm{d}}{\mathrm{d}x}\{V(x)t(x)\} - \frac{\mathrm{e}}{\hbar}B_\perp(x)t(x)\,. \tag{5.4}$$

When the sample has uniform thickness and composition, the first term in Eq. 5.4 is zero, and the phase gradient can be interpreted directly in terms of the in-plane magnetic induction. However, in many cases, the projected thickness or the composition of the magnetic sample may vary rapidly. In such cases, the first mean inner potential term $V(x)t(x)$ is likely to dominate both the phase and the phase gradient. Attempts to quantify the magnetization in the sample then become complicated, and additional processing is required before the in-plane magnetization can be extracted.

When two coherent objects and reference waves interfere to produce a hologram, the intensity distribution in the holographic interference fringe pattern takes the form

$$\begin{aligned} I(x, y) &= |\Psi_1(x, y)|^2 + |\Psi_2(x, y)|^2 + |\Psi_1(x, y)|\,|\Psi_2(x, y)| \\ &\quad \times \left(\mathrm{e}^{\mathrm{i}(\Phi_1 - \Phi_2)} + \mathrm{e}^{-\mathrm{i}(\Phi_1 - \Phi_2)}\right) \\ &= A_1^2 + A_2^2 + 2A_1A_2\cos(\Delta\phi)\,, \end{aligned} \tag{5.5}$$

where Ψ is the electron wavefunction, $\Delta\phi$ is the phase change of the electron wave, and the subscripts refer to the reference and object waves. Thus, a series of cosinusoidal fringes is superimposed onto a normal TEM bright field image. The relative phase shift of the electron wave after passing through the sample is represented by shifts in the positions and spacings of the interference fringes. Finite beam divergence (effective source size) and energy spread (temporal coherence) cause loss of contrast in the interference fringes, which, in turn, affects the precision and accuracy of the reconstructed holographic phase image.

Figure 5.2 provides an illustration of the recording and processing steps. The off-axis electron hologram at the top left (Fig. 5.2a) corresponds to a chain of magnetite nanocrystals originating from a single magnetotactic bacterial cell, which is supported on a holey carbon film. A region of vacuum outside the specimen is located in the upper left-hand corner of the hologram. Large deviations in the spacing and the angle of the fringes occur as they cross the crystallites, and these variations can be interpreted in terms of the phase shift of the electron wavefunction relative to the reference vacuum wave. By Fourier transforming the hologram, a two-dimensional frequency

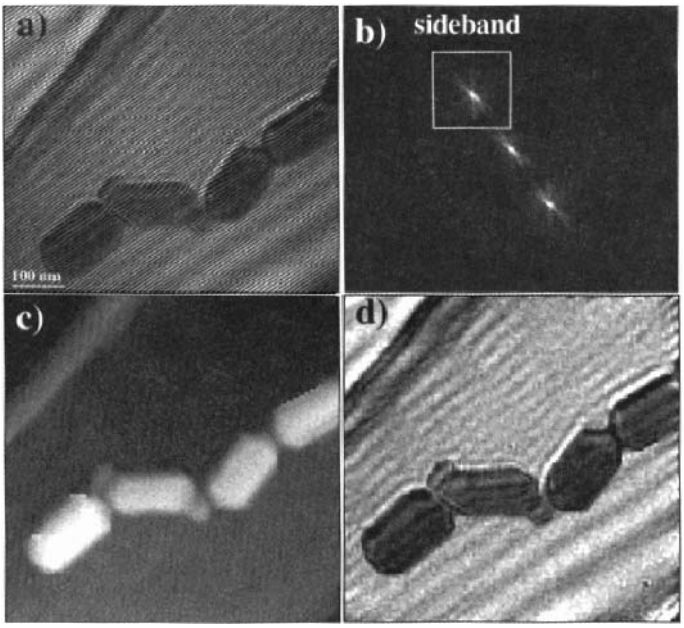

Fig. 5.2. (**a**) Off-axis electron hologram showing chain of magnetite nanocrystals; (**b**) Fourier transform of (**a**), indicating sideband used in phase reconstruction; (**c**) reconstructed phase image; (**d**) reconstructed amplitude image

map is obtained, as shown in Fig. 5.2b. The two strong sideband spots correspond to the fundamental cosine frequency. Their separation is due to the relative tilt of the object and reference waves, which depends on the voltage applied to the biprism. The intensity variations around the spots reflect the local phase shifts of the electron wavefunction caused by the sample. The phase of the image wave cannot be obtained from the central autocorrelation function, but the sidebands, which are complex conjugates of each other, contain this information. The reconstruction process makes use of either one of these sidebands, hence the term "off-axis" holography. This off-axis approach provides a convenient solution to the problem of overlapping twin images, which is a serious issue for in-line holographic techniques [6].

Hologram reconstruction involves the extraction and re-centering of one of the sidebands, followed by the calculation of its inverse Fourier transform. The amplitude and phase of the resulting complex image are then

$$\begin{aligned} \phi &= \arctan(\mathrm{i}/r) \\ A &= \mathrm{sqrt}\left(r^2 + \mathrm{i}^2\right) , \end{aligned} \tag{5.6}$$

where r and i are the real and imaginary parts of the wavefunction, respectively.

Figures 5.2c and 5.2d show the corresponding reconstructed phase and amplitude, respectively, of the hologram shown in Fig. 5.2a. The phase is usually calculated modulo 2π, which means that 2π phase discontinuities that are unrelated to particular

specimen features may appear at positions in the phase image where the phase shift exceeds this amount. Suitable phase-unwrapping algorithms must then be used to unwrap the phase and to ensure reliable interpretation of the image features [14]. In addition, reference holograms are usually recorded with the sample removed. Any artifacts associated with local imperfections or irregularities of the imaging and recording systems are then excluded by dividing the sample wavefunction by the reference wavefunction before recovering the amplitude and phase.

5.2.2 Experimental Setup

Our attention here is focused on the off-axis mode of electron holography since this mode has been used almost exclusively in electron microscope studies of magnetic materials. The microscope geometry for off-axis electron holography in the TEM is illustrated schematically in Fig. 5.1. Equivalent configurations can also be achieved in the scanning TEM using a stationary defocused probe [6,16]. The sample is examined using defocused, coherent illumination, usually from a FEG electron source, and it is positioned so that it covers approximately half the field of view. The electrostatic biprism is usually a thin ($< 1\mu$m) metallic wire or quartz fiber coated with gold or platinum, which is biased by means of an external dc power supply or battery. The application of a voltage to the biprism causes overlap between the object wave and the vacuum or reference wave, resulting in the formation of the holographic interference pattern on the final viewing screen or detector. Voltages of between 50 and 200 V are typically used for the medium-resolution examples shown below, but higher voltages are required for higher-resolution applications [17]. A rotatable biprism is highly useful since it is often necessary to align the direction of the interference fringes with particular sample features of interest.

Although the biprism may be located in one of several positions along the beam path, the usual position is in place of one of the selected-area apertures. In this configuration, the holographic interference pattern that is formed at the first image plane must be translated electron-optically below the selected area plane. This is achieved by increasing the excitation of the diffraction or intermediate lens so that the image is located below the biprism. The interference fringe spacing and the width of the fringe overlap region are usually then referenced to the image magnification in this plane [18], which, in turn, depends on the method used to ensure that the magnetic sample is located in a field-free region. For example, a low magnification and a correspondingly large field of view are obtained when the normal objective lens is turned off. A post-column imaging filter can then be used to obtain additional magnification, but the image resolution is relatively poor because the imaging intermediate lens is only weakly excited. An alternative approach is to use a modified specimen holder, with the sample located just outside the field of the immersion objective lens. A far-out-of-focus image is then obtained, but the phase-shifting effects due to the objective lens defocus can be corrected during the reconstruction process [16]. Yet another approach involves the use of a weak imaging lens below the normal objective lens. The so-called “Lorentz” minilens of the Philips CM200 FEG-TEM allows image magnifications of up to 70,000x to be obtained, and the

reconstructed phase image can have a spatial resolution equal to the 1.4 nm line resolution of the lens [19]. A special low-field ($\sim$ 5.5 G) objective lens for studying small magnetic particles has been reported to provide a maximum magnification of 500 000x [20].

Alternatively, by placing the biprism in one of the condenser aperture positions preceding the sample, a very different configuration is obtained that is equivalent to creating two closely spaced, overlapping plane waves incident on the sample [21]. An equivalent mode can be obtained by using the stationary focused probe of the STEM [16]. By defocusing the observation plane relative to the sample, differences in phase shift between adjacent areas are recorded in the interference pattern, resulting in a differential phase contrast (DPC) image. Either a rotating biprism or a rotating sample holder must be used in this configuration to enable both components of the in-plane magnetic field to be characterized. This approach has the disadvantages that any one hologram only contains information about one component of the magnetization and the spatial resolution of the recovered phase is limited because the image is defocused. However, this DPC imaging mode is particularly attractive for low magnification holography applications because the need for a vacuum reference wave is eliminated, thus making it easier to prepare suitable specimens.

5.2.3 Practical Considerations

The coherence of the electron beam is all-important for practical electron holography. The beam convergence angle must be minimized as far as practicable to avoid loss of phase detail in the reconstructed hologram stemming from poor interference fringe contrast. Even with a FEG source, it is common practice to employ illumination that is deliberately made to be highly elliptical using appropriate condenser lens stigmator settings. Aspect ratios of 100:1 are not uncommon [18]. The major axis of the elliptical illumination patch must also be aligned perpendicular to the biprism wire direction to maximize the coherence and fringe contrast.

Further experimental factors impact the reconstruction process. Higher biprism voltages result in smaller fringe spacings (needed for small object dimensions) and larger fringe overlap width (greater field of view). However, fringe contrast typically drops off as the biprism voltage is increased, and higher magnifications are required to avoid insufficient sampling of the finely spaced interference fringes by the recording system. A common rule of thumb is that four effective pixels per hologram fringe is the minimum acceptable sampling [22], although for sensitive phase measurements even greater sampling rates are recommended [18].

When quantitative analysis of phase shifts is required, holograms should be recorded using electron detectors that have linear output over a large dynamic range. The CCD camera is ideal for this purpose, and subsequent computer processing is also facilitated by digital acquisition [13, 23]. Note that the sampling density of the recovered amplitude and phase is determined by the effective pixel size of the hologram. The size of the sideband extracted during hologram reconstruction can also affect the final resolution of the phase image. In situations

where a Lorentz lens has been used for holographic imaging, aberrations of the lens do not usually limit the spatial resolution of the final reconstructed image. The strength of the magnetic signal and the phase sensitivity of the hologram (i.e., the signal-to-noise ratio in the phase image) are more often the factors that limit the resolution for magnetic materials. Phase sensitivities of $2\pi/100$ can be achieved routinely during holographic studies using quantitative recording and processing [13]. It is then possible to detect magnetic details in thin films on a scale of about 5 nm [24]. Thicker films, larger magnetic fields, or longer acquisition times are necessary for recording smaller features using instrumentation that is currently available.

5.2.4 Applications

Off-axis electron holography has been used successfully in a variety of applications. Electron holography was originally proposed by Gabor [25] as a means of correcting electron microscope lens aberrations. Instrumental factors (primarily the coherence of the electron source) prevented his goal from being realized for many years. Optical methods [26,27] and computer reconstruction (e.g., [17,28]) have been used to surpass conventional microscope resolution limits.

Off-axis electron holography has also been used in many studies related to electrostatic fields. For example, reverse-biased p-n junctions were studied [29] at low magnification ($\sim$ 2500x), and electrostatic fields associated with charged latex spheres were also investigated [30]. Depletion region potentials at a Si/Si *p-n* junction were reported [31], and the two-dimensional electrostatic potential associated with deep-submicron transistors has been mapped at a resolution of $\sim$ 10 nm and a sensitivity approaching 0.1 V [32]. An improvement in spatial resolution to $\sim$ 5 nm has been achieved in studies of 0.13 μm device structures [33]. The electrostatic potential and associated space charge across grain boundaries in $SrTiO_3$ has also been reported [34]. Recently, attention has turned to the (Ga, In, Al)N system. Examples include the observation of piezoelectric fields in GaN/InGaN/GaN strained quantum wells [35] and the mapping of electrostatic potentials across an AlGaN/InGaN/AlGaN heterojunction diode [36].

Investigations of magnetic materials by electron holography have historically been limited to spatial resolutions of considerably more than 10 nm due to the obvious requirement for the sample to be located in a region of very low external field to prevent magnetization saturation. Typically, the strong objective lens has been switched off, so that imaging was restricted to the diffraction/projector system of lenses below the sample. Significant applications have included experimental confirmation of the Aharonov-Bohm effect at low temperature [37], studies of vortex "lattices" in a superconductor [38], and observations of thin magnetized Co film used for magnetic recording applications [39]. Further applications of electron holography to magnetic materials are described in the following sections.

5.3 Applications to Magnetic Materials

5.3.1 FePt Thin Films

Anisotropic magnetic films that have either longitudinal (in-plane) or perpendicular (out-of-plane) magnetization are of central importance to the magnetic recording industry. Ordered alloys of Fe-Pt and Co-Pt with the $L1_0$ crystal structure have this desired magnetocrystalline anisotropy and large magnetic moments. Spontaneous ordering of Fe-Pt can occur during deposition, causing development of the ordered phase [40]. The tetragonal *c*-axis is then predominantly either out of the plane or in-plane, depending on the particular substrate used for growth. Figure 5.3 shows results from a study of an epitaxial $Fe_{0.5}Pt_{0.5}$ ordered alloy [19] that had been deposited using molecular beam epitaxy onto an MgO (110) single-crystal substrate. In this growth direction, the anisotropic $L1_0$ ordered alloy phase has the (001) easy axis parallel to the film normal. The reconstructed phase image in Fig. 5.3b clearly shows the presence of magnetic fringing fields outside the material, and the induction map in Fig. 5.3c confirms that adjacent domains within the FePt film have opposite polarity.

This study highlights some of the difficulties associated with using electron holography to quantify the distribution of magnetic flux in vacuum. The technique will always be insensitive to any magnetic field component that is parallel to the electron beam direction. Moreover, the information contained in a recorded hologram represents a two-dimensional projection of a three-dimensional field. Extensive calculations were thus required, for example, in order to quantify the magnetic field from the tip of a magnetic force microscope [41], and further tomographic experiments were needed to confirm the cylindrical symmetry that was assumed in the calculations [42]. Full three-dimensional simulations will always be needed for quantitative interpretation in situations where the fringing fields extend relatively large distances into vacuum [43, 44].

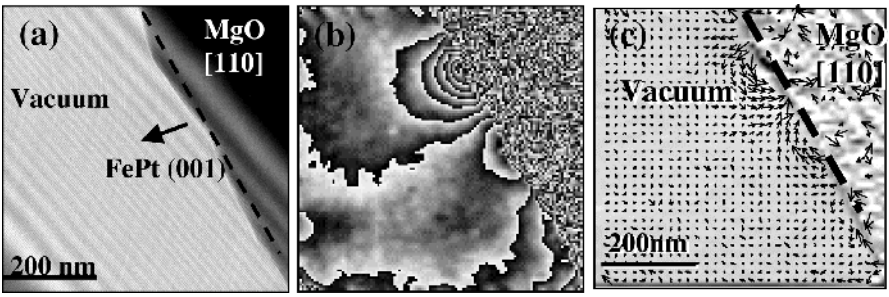

Fig. 5.3. (**a**) Off-axis electron hologram obtained from epitaxial FePt/MgO with (001) easy axis parallel to film normal; (**b**) contoured phase image showing magnetic flux extending into vacuum; (**c**) induction (arrow) map confirming opposite polarity of adjacent FePt domains

5.3.2 NdFeB Hard Magnets

Hard magnetic materials such as NdFeB alloys have high magnetic remanence and coercivity that lead to many practical applications. Off-axis electron holography has been used to image the magnetic induction in $Nd_2Fe_{14}B$ with nanometer-scale resolution and high signal-to-noise [45–47]. As a representative example, Fig. 5.4 shows reconstructed phase images obtained from a sample of die-upset $Nd_2Fe_{14}B$ that was prepared for electron microscopy observation by standard dimpling and ion-milling. A variety of serpentine and "Y"-shaped domains that extend to the sample edge are visible in Fig. 5.4a: These domain shapes are similar to those previously observed at grain boundaries in sintered NdFeB [48]. After heating the sample to a nominal temperature of 300 °C and subsequent cooling to room temperature, rearrangement of these domains occurred, as visible in Fig. 5.4b. The well-defined domains on the left-hand side have disappeared, and reduced phase gradients indicate that the remaining structure has a large out-of-plane component. Domain walls have been released from the thin edge of the sample, although some remaining domains were found to have interacted with structural features that were identified as planar defects and grain boundaries. Further heating to 400 °C, which is above the Curie temperature of 312 °C [49], resulted in the complete disappearance of the domain structure. A single pixel line scan across the central part of Fig. 5.4a put an upper limit of 10 nm on the domain wall width. This result agreed well with theoretical values [50], particularly bearing in mind that no special care was taken to ensure that the walls were parallel to the electron beam path.

In order to map the magnetic induction within the sample, simple gradients of the phase image at $\pm 45^\circ$ angles were calculated according to Eq. 5.4. These two gradient images were then combined to form a vector map, thereby producing a direct image of the magnetic induction within the domains, as shown in Fig. 5.5. The vector map in Fig. 5.5a is divided into 20 nm × 20 nm squares, and a low contrast image of the x-gradient has been superimposed for reference. The minimum vector length is zero (which is indicative of out-of-plane induction), while the maximum vector length, as calculated from the modulus of the gradients near the center of the image, corresponds to $4\pi M_s = B = 1.0$ T for an estimated sample thickness of 90 nm. The

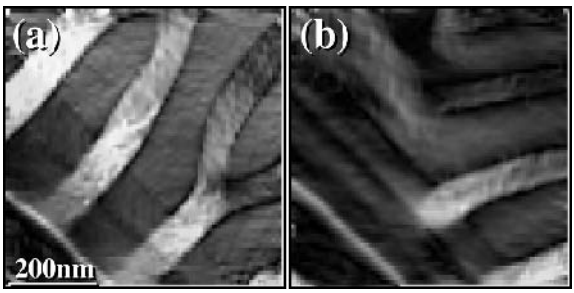

Fig. 5.4. Reconstructed phase images from $Nd_2Fe_{14}B$ sample: (**a**) before, and (**b**) after heating to 300 °C

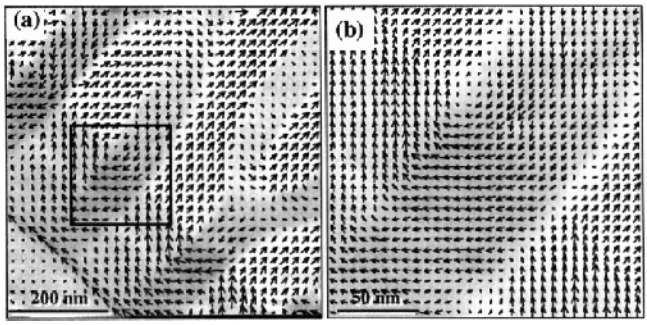

Fig. 5.5. (**a**) Induction map derived from gradients of phase image shown in Fig. 5.4; (**b**) enlargement of area indicated in (**a**) showing singularities and domain wall character

vector map shows that the magnetizations of the domains in this sample region are oriented at approximately 90° to each other, rather than 180°, as might be expected for a material having such strong uniaxial anisotropy. The domains near the sample edge close the in-plane induction more or less parallel to the thin edge. Note also the pairs of singularities at the intersection with the striped domains, which are reminiscent of cross-tie walls that contain periodic arrays of Bloch-lines of alternating polarity [50].

A vector map of the area outlined in Fig. 5.5a is shown at higher magnification in Fig. 5.5b. This map is divided into 6.7 nm × 6.7 nm squares with a maximum vector length again corresponding to 1.0 T. Portions of the domain walls that run perpendicular to the sample edge show distinct out-of-plane character, and there is an apparent tendency for the induction in the center domain to rotate toward a 180° orientation near the vortices. The vortices show Bloch-like character with vanishingly small vector length, indicating small in-plane components. The majority of the 90° walls show large in-plane components, as expected for a thin sample. However, it is emphasized that care is needed when interpreting fine details in such induction maps, due to the undetermined effects of the fringing fields immediately above and below the sample surfaces. Moreover, caution is needed when extrapolating the magnetization states of thin films to bulk materials. The need for an electron-transparent sample should always raise concerns about reliability whenever a bulk magnetic material is thinned for TEM examination.

5.4 Magnetic Nanostructures

5.4.1 Co Spheres

In small magnetic particles, the energy associated with the formation of domain walls becomes an increasingly large contribution to the total magnetostatic energy of the entire particle. Domain walls are then less likely to be observed within small particles when they are in their remanent state. Moreover, because of the limited resolution of most magnetic imaging techniques, it becomes increasingly difficult to characterize

micromagnetic structure. Electron holography thus has an opportunity to provide unique experimental information unobtainable with other techniques. For example, isolated polyhedral particles of barium ferrite, with sizes ranging from about 0.1 to 1.0 μm, were studied using electron holography [51]. On the basis of the magnetic-flux-line geometry surrounding the particles, it was concluded that these existed as single magnetic domains. However, flux lines *within* the ferrite particles, and also in smaller-sized iron particles, were not identified in this early study, presumably because the dominant influence of the mean-inner-potential contribution to the phase and phase gradients could not be extracted (see Eqs. 5.3 and 5.4). It is our experience that information about the thickness profile of small particles must be obtained before their internal magnetization can be determined [52]. In some special geometries, such as for CrO_2 needles [53], the particle cross sections may be constant, thus allowing thickness variations to be neglected.

In some magnetic nanostructures, large variations in the projected thickness of the sample are unavoidable. Figure 5.6 shows an off-axis electron hologram obtained from a chain of carbon-coated spherical Co particles [54], and Fig. 5.6b shows the corresponding reconstructed phase image. Holographic analysis shows that the magnetic contribution to the phase shift of the Co particle along the line labeled "1" results in a difference in the value of the phase in vacuum on each side of the sphere. However, it is clear that the mean inner potential makes the dominant contribution to the phase profile. In this particular study, extensive modeling taking account of the

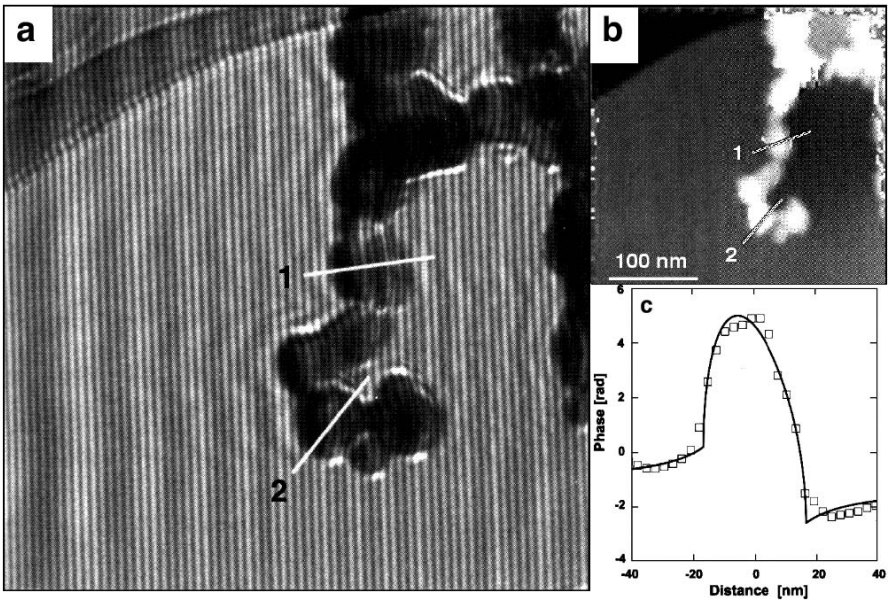

Fig. 5.6. (**a**) Hologram of chain of carbon-coated Co spheres; (**b**) reconstructed phase image; (**c**) phase profile along line in phase image in (**b**) (open squares). Solid line shows fitted phase shift calculated for an isolated sphere

particle shape was required before quantitative analysis of the magnetization within the crystalline nanoparticles could be completed.

5.4.2 Magnetotactic Bacteria

Certain sample geometries lend themselves to unidirectional remanent states, and phase shifts due to sample thickness and electrostatic effects can then be easily separated from those due to magnetostatic effects. Magnetization reversal can be accomplished *in situ* within the microscope by tilting the sample in the applied field of the conventional microscope objective lens. The external field is then removed, and separate holograms are recorded with the induction in the sample in two opposite directions [52]. The sum of the phases of these two holograms provides twice the mean inner potential contribution to the phase if the magnetization has reversed exactly (See Eqn. 5.3), while the difference between the phases provides twice the magnetic contribution. As an example of this procedure, Fig. 5.7a shows a hologram of a chain of magnetite crystals from a single cell of the aquatic magnetotactic bacterium *Magnetospirillum magnetotacticum*. Following magnetization reversal and addition of the phases, the electrostatic contribution is extracted as shown in Fig. 5.7b: the thickness contours reveal the crystallites to be cubocathedral in shape [55]. The magnetic contribution to the phase is shown in Fig. 5.7c. The phase contours are parallel to lines of constant magnetic induction integrated in the incident beam direction and have been overlaid onto the mean inner potential contribution to the phase so that the positions of the crystals and the magnetic contours can be correlated.

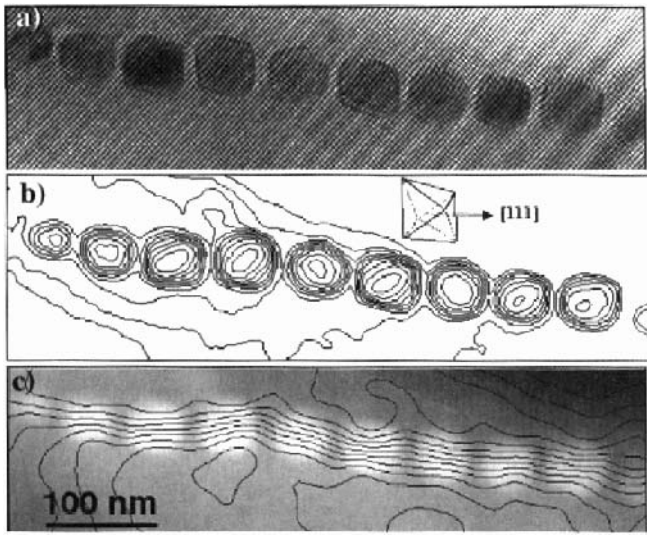

Fig. 5.7. (**a**) Hologram of chain of magnetite crystals in Magnetospirillum Magnetotacticum; (**b**) mean inner potential contribution to phase of reconstructed hologram. Thickness contours indicate cuboctahedral shape; (**c**) magnetic contribution to phase

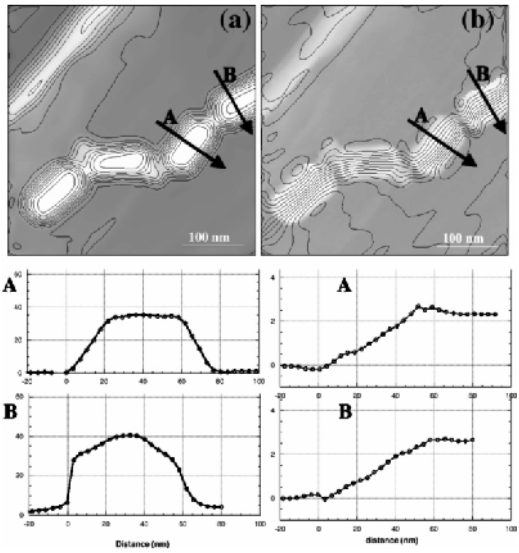

Fig. 5.8. (**a**) Thickness map and (**b**) phase contour map from part of a chain of magnetite magnetosomes from bacterial strain Itaipu 3. Line profiles along lines "A" and "B" are shown below the images

In this way, the magnetic flux both within and in between the crystallites becomes visible, and the total magnetic dipole moment of the particle chain can also be determined.

Further holography studies of magnetotactic bacteria have been reported [56, 57]. Single cells from two different bacterial strains, designated as MV-1 and MS-1, consisted of magnetite crystals that were ~ 50 nm in length and arranged in chains. Analysis revealed that the individual crystals existed as single magnetic domains [56], as anticipated from numerical micromagnetic modeling, which predicted that the transition to a multi-domain state should occur at a size of ~ 70 nm for cube-shaped particles [58]. Furthermore, by careful monitoring of the phase shifts measured across the chain as a function of applied field, the coercive field was determined to be between 300 and 450 Oe. Similar analysis has been applied to chains of larger magnetosomes identified as Itaipu 1 and Itaipu 3 [57]. Figures 5.8a and b, respectively, show thickness and phase contour maps from part of a chain of Itaipu 3 magnetosomes. The corresponding line profiles along the lines designated "A" and "B" are shown directly underneath these two images. Such thickness profiles can be used to determine particle morphologies, and their magnetizations can then be determined from the phase maps.

5.4.3 Patterned Nanostructures

Because of their potential utilization for information storage, there is much current interest in the magnetization reversal of individual magnetic nanostructures. Due to

their small size, magnetostatic energy contributions have a major influence in determining their overall magnetic response. Further important factors include individual particle geometries, as well as their proximity to other particles. We have used off-axis electron holography to investigate the micromagnetic behavior of a wide range of nanostructured elements. This approach enables the magnetization state to be visualized during hysteresis cycling [59–63].

Elements of various shapes, sizes, and separations were prepared by electron-beam evaporation onto self-supporting 55-nm-thick silicon nitride membranes using standard electron-beam lithography and lift-off processes [61]. Magnetic fields were applied by tilting the sample in situ within the microscope and then using the conventional microscope objective lens to obtain the desired field. The hysteresis loops of individual elements could thus be determined, and the extent of any interactions between closely-spaced elements could also be assessed.

The application of electron holography enabled flux lines both inside and outside the elements to be visualized even though substantial loss of interference-fringe contrast occurred due to the presence of the underlying silicon nitride support. The results of holographic reconstruction for two closely spaced Co rectangles over a complete hysteresis cycle, working in a counter-clockwise direction, are shown in Fig. 5.9. (The in-plane components of the applied field are indicated in each image.) The separation of the phase contours is proportional to the magnetic induction integrated in the incident beam direction. The fringing fields extending between elements are only minimized when the field lines are located entirely within both elements. The characteristic solenoidal shape then observed is indicative of flux closure associated with a vortex state.

Micromagnetic simulations based on the Landau-Lifshitz-Gilbert equations were made to aid in the interpretation of the phase profiles [60]. Reasonable agreement with the experimental results was obtained, although further analysis revealed subtle but important differences. Simulated vortices matched the experimental results except that they were formed at higher fields in the simulations, presumably because of local defects or inhomogeneities in the real elements. The simulated results were also affected by the squareness of the element corners, and slight changes in the initial state had a strong influence on subsequent domain formation during switching. Simulations also confirmed that the strength and direction of the applied field had a marked impact on the observed domain structure [60], thus emphasizing the need to correlate experimental measurements with micromagnetic simulations. Figure 5.10 compares simulations for two cells simulated as a pair (left set) and simulated separately (although displayed as a pair). The different domain configurations visible for the smaller cell in this figure demonstrate convincingly that the magnetization behavior of the adjacent Co elements is affected by their mutual proximity and interaction. Intercell coupling is clearly an important factor that must not be overlooked when designing magnetic storage devices with very high density.

A further important consideration for the design of magnetic elements for device applications is the formation of remanent states from different stages in a magnetization reversal loop. In normal operation, the storage element must first be magnetized and the external field then removed, the objective being to retain a non-solenoidal dis-

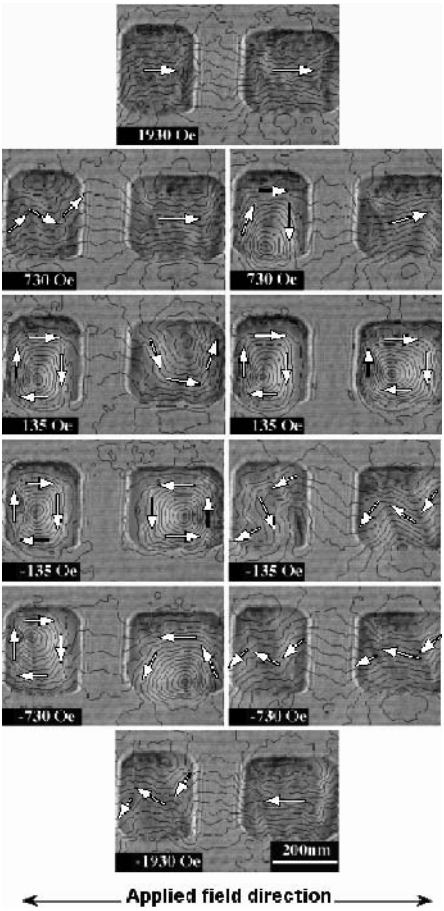

Fig. 5.9. Magnetic contributions to phase for 30-nm-thick Co elements over hysteresis cycle. Phase contours are separated by 0.21π radians. Field was applied in horizontal direction of figure, and loop should be followed counter-clockwise. Average out-of-plane field of 3600 Oe directed into the page

tribution. As shown by the representative examples in Fig. 5.11, none of the different remanent states of the two Co elements showed the non-solenoidal domain structures visible at the extreme ends of the hysteresis loop. Indeed, new and unexpected domain configurations were sometimes observed such as the double-vortex structure visible in the larger rectangle. It is possible that the presence of the external vertical field caused these states to be stable, Nevertheless, the value of experimental observations, and the need for reproducibility in the formation of remanent states, are emphasized.

Further studies of patterned nanostructures have focused on submicron Co (10 nm)/Au (5 nm)/Ni (10 nm) "spin-valve" (SV) elements shaped as rectangles, diamonds, ellipses, and bars with lateral dimensions on the 100-nm scale [61,63]. Similar

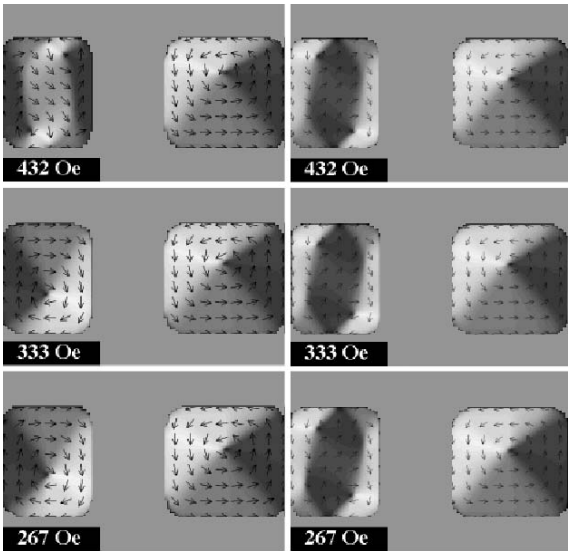

Fig. 5.10. Micromagnetic simulations for 30-nm-thick Co rectangles with 3600 Oe field directed into page, rounded bit corners, and applied fields as indicated. Left set simulated for two cells together. Right set simulated for cells separately (but shown together)

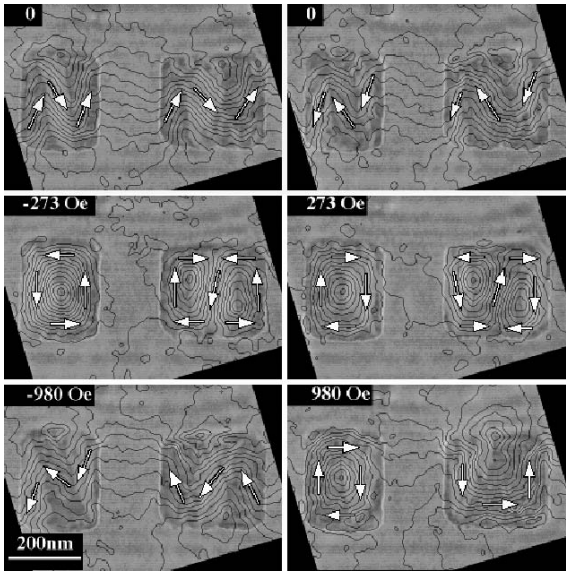

Fig. 5.11. Remanent states for 30-nm-thick Co elements. Left column: in-plane fields applied directly after large positive in-plane field. Right column: starting with large negative in-plane

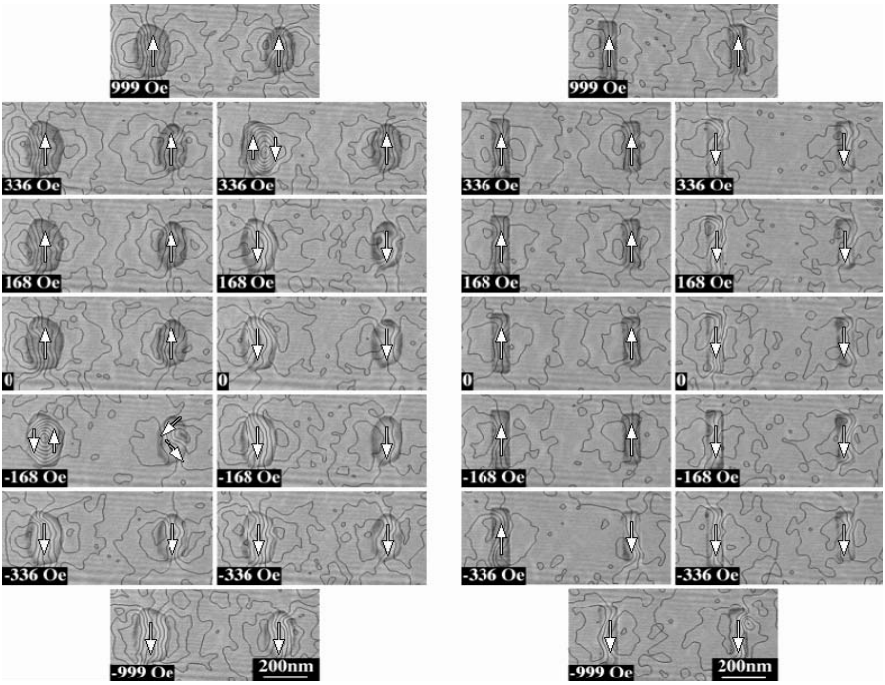

Fig. 5.12. Magnetic contributions to phase for elliptical and bar-shaped Co(10 nm)/Au (5 nm)/Ni(10 nm) spin-valve elements over complete hysteresis cycle. Phase contours of 0.064π radians. Field applied in vertical direction. Loop should be followed counter-clockwise. Average out-of-plane of 3600 Oe directed into the page

SV layered structures are the subject of much current research and development activity because of the large differences in resistance obtained when the magnetization directions of the two magnetic layers are aligned either parallel or anti-parallel. The understanding and control of magnetization reversal in such layered combinations is essential for future information storage applications. Representative results from a complete hysteresis cycle for elliptical and bar-shaped elements are shown in Fig. 5.12. The direction of the in-plane component of the applied field is aligned along the long axis of each element, and the arrows within each element indicate the field direction. It was notable in additional studies of rectangular SV elements that, unlike some of the magnetization states during hysteresis cycling, vortex states were not visible in any of the remanent states. Micromagnetic simulations later suggested that this difference in behavior was most likely due to the presence of strong coupling between the Co and Ni layers within each element. It was also interesting that the smaller diamond-shaped elements had a substantially larger switching field, which could possibly be attributed to an increased difficulty in nucleating end domains that initiate magnetization reversal [64].

A significant observation made in these SV studies was the occurrence of two different contour spacings within each element at different applied fields, with corresponding steps in the hysteresis loops. Micromagnetic simulations, described in detail elsewhere [63], indicate that coupling between the Co and Ni layers accounted for this behavior. The Ni layer in each element reverses its magnetization direction well before the external field reaches 0 Oe. Thus, an antiferromagnetically coupled state, caused by the strong demagnetization field of the closely adjacent and magnetically more massive Co layer, must be the remanent state of these Co/Au/Ni SV elements. Flux closure associated with an antiferromagnetic state could also contribute to the absence of end domains, which are commonly observed in thicker single layer films of larger lateral dimensions. Solenoidal states were observed experimentally for both elliptical and diamond-shaped elements, but they could not be reproduced in the simulations. Structural imperfections such as crystal grain size or orientation are factors that could contribute to this difference in behavior.

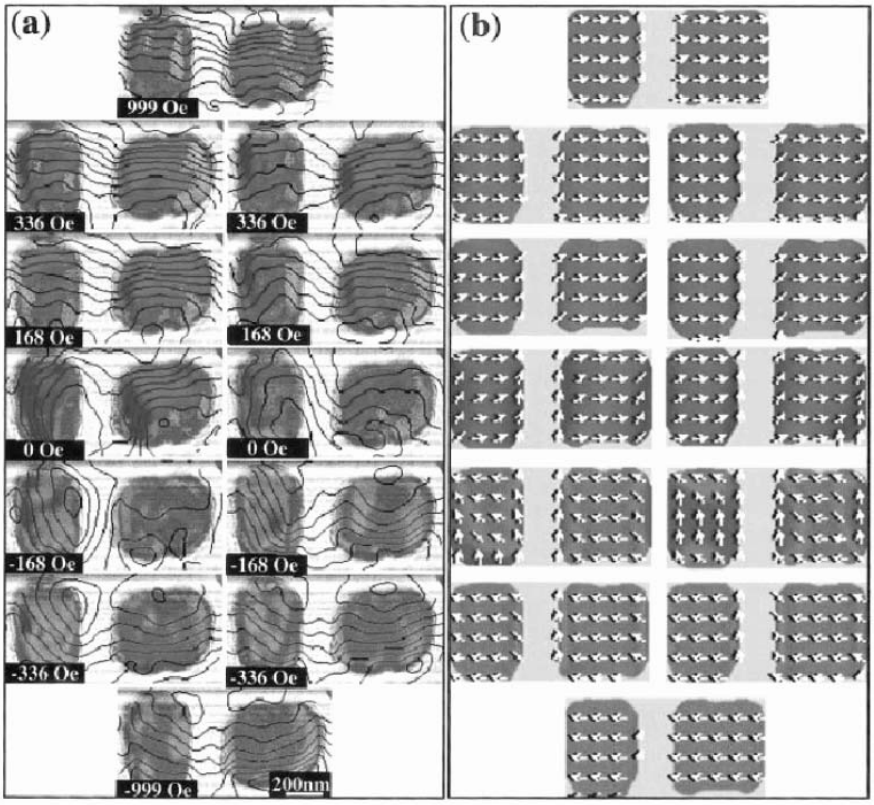

Fig. 5.13. Comparison of experimental and simulated magnetization states for exchange-biased CoFe/FeMn patterned nanostructures over complete magnetization reversal cycle. Applied in-plane field as shown directed along horizontal axis. Phase contours of 0.085 radians

In practical SV applications, it is usual to pin, or "exchange bias," the magnetization direction of one of the magnetic layers using an adjacent antiferromagnetic layer such as FeMn [65]. Off-axis electron holography has been combined with micromagnetic simulations to investigate magnetization reversal mechanisms and remanent states in exchange-biased submicron CoFe/FeMn nanostructures [61, 62]. Figure 5.13 compares a typical experimental hysteresis loop with micromagnetic simulations, proceeding in a counter-clockwise direction with the in-plane applied field directed along the horizontal direction. No solenoidal or vortex states are observed, and complete reversal is not achieved, suggesting that shape anisotropy has a controlling influence on the response. Smaller and larger elements behaved quite differently, again implying the likely dominant role of shape anisotropy.

5.5 Outlook

The results described here convincingly demonstrate that off-axis electron holography has a valuable role to play in understanding the complex behavior of real magnetic nanostructures. The technique enables both visualization and quantification of magnetic fields with high spatial resolution and sensitivity. The theoretical basis for the technique is well established, and experimental applications to important materials are starting to be explored. As field-emission-gun TEMs become increasingly available, it can be anticipated that electron holography will develop into a widely used tool for micromagnetic characterization.

A major challenge for the technique is to provide direct visualization of dynamic effects induced by variations of the magnetic field, which are needed for a full understanding of micromagnetic behavior. The problem for the microscopist is that when changes are made to the applied field, the electron trajectories through the objective lens are seriously affected, and the holographic interference process is also likely to be impacted. Our experiments have involved tilting the sample in situ within the field of the weakly excited objective lens to change the in-plane field component [59]. However, the out-of-plane component of the applied field has been shown to impose switching asymmetries during hysteresis cycling of Co nanostructures [60]. An alternative, and obviously preferable, solution would be to provide three sets of auxiliary coils: One set would be used to apply the field at the sample level, and the subsequent sets would be used to steer the beam back onto the optic axis [66]. This possibility is not yet generally available.

The technique of off-axis electron holography is not well-suited to real-time observations because the holograms are usually processed off-line. One approach used to circumvent this problem has been to feed the signal from an intensified TV camera to a liquid crystal (LC) panel, which was then used to provide the input for a light-optical reconstruction [67]. However, geometric distortions may result from the TV camera and the LC panel, and reference holograms are not conveniently available to correct these distortions, unlike the situation for digital recording and processing. The dynamic behavior of magnetic domains in a thin permalloy film has been observed in real time using this type of system [51]. As faster computers

and better CCD cameras become available, real-time viewing of reconstructed phase images may soon become possible.

Acknowledgement. Much of the electron holography described here was carried out at the Center for High Resolution Electron Microscopy at Arizona State University. We are grateful to Drs. R.F.C. Farrow, R.B. Frankel, B. Kardynal, S.S.P. Parkin, M. Posfai, M.R. Scheinfein, and Y. Zhu for provision of samples and ongoing collaborations.

References

1. J.P. Jakubovics (1976) In: Lorentz Microscopy and Applications (TEM and SEM). U. Valdre and E. Ruedl (eds) Electron Microscopy in Materials Science, Part IV, Commission of the European Communities, Brussels, p. 1303.
2. J.N. Chapman, J. Phys. D: Appl. Phys. **17**, 623 (1984).
3. S. McVitie and J.N. Chapman, Microscopy and Microanalysis **3**, 146 (1997).
4. H. Lichte, Adv. Opt. Electron Micros. **12**, 25 (1991).
5. A. Tonomura (1993) Electron Holography, Springer Series in Optical Sciences, Vol. **70**. Springer, Heidelberg.
6. J.M. Cowley, Ultramicroscopy **41**, 335 (1992).
7. G. Möllenstedt and H. Düker, Naturwissen. **42**, 41 (1955).
8. M.E. Haine and T. Mulvey, J. Opt. Soc. Amer. **42**, 763 (1952).
9. A. Tonomura, T. Matsuda, and J. Endo, Jpn. J. Appl. Phys. **18**, 1373 (1979).
10. A. Tonomura, Rev. Mod. Phys. **59**, 639 (1987).
11. E. Völkl and M. Lehmann, The reconstruction of off-axis electron holograms, In: E. Völkl, L.F. Allard, and D.C. Joy (eds.), Introduction to Electron Holography, Kluwer Academic, New York. pp. 125–151.
12. W.J. de Ruijter, Micron **26**, 247 (1995).
13. W.J. de Ruijter and J.K. Weiss, Ultramicroscopy **50**, 269 (1993).
14. D.J. Smith, W.J. de Ruijter, J.K. Weiss and M.R. McCartney (1999) Quantitative electron holography, In: E. Völkl, L.F. Allard, and D.C. Joy (eds.), Introduction to Electron Holography. Kluwer Academic, New York. pp. 107–124.
15. M. Gajdardziska-Josifovska, M.R. McCartney, W.J. de Ruijter, D.J. Smith, J.K. Weiss, and J.M. Zuo, Ultramicroscopy **50**, 285 (1993).
16. M. Mankos, A.A. Higgs, M.R. Scheinfein and J.M. Cowley, Ultramicroscopy **58**, 87 (1995).
17. A. Orchowski, W.D. Rau, and H. Lichte, Phys. Rev. Lett. **74**, 399 (1995).
18. D.J. Smith and M.R. McCartney (1999) Practical electron holography, In: E. Völkl, L.F. Allard and D.C. Joy (eds) Introduction to Electron Holography. Kluwer Academic, New York. pp. 87–106.
19. M.R. McCartney, D.J. Smith, R.F.C. Farrow, and R.F. Marks, J. Appl. Phys. **82**, 2461 (1997).
20. T. Hirayama, J. Chen, Q. Ru, K. Ishizuka, T. Tanji, and A. Tonomura, J. Electron Microsc. **43**, 190 (1994).
21. M.R. McCartney, P. Kruit, A.H. Buist, and M.R. Scheinfein, Ultramicroscopy **65**, 179 (1996).
22. D.C. Joy, Y.-S. Zhang, X. Zhang, T. Hashimoto, R.D. Bunn, L.F. Allard, and T.A. Nolan, Ultramicroscopy **51**, 1 (1993).

23. J.M. Zuo, M.R. McCartney, and J.C.H. Spence, Ultramicroscopy **66**, 35 (1997).
24. H. Lichte, H. Banzhof, and R. Huhle, In: Electron Microscopy 98, Vol. 1, H.A. Calderon Benavides and M.J. Yacaman (eds.), (IOP, Bristol, 1998) pp. 559–560.
25. D. Gabor, Proc. Roy. Soc. London, A**197**, 454 (1949).
26. A. Tonomura, T. Matsuda, J. Endo, H. Todokoro, and T. Komoda, J. Electron Micr. **28**, 1 (1979).
27. H. Lichte, Ultramicroscopy **20**, 293 (1986).
28. W.D. Rau and H. Lichte (1999) High resolution off-axis electron holography, In: E. Völkl, L.F. Allard, and D.C. Joy (eds.). Introduction to Electron Holography, Kluwer Academic, New York, pp. 201–229.
29. S. Frabboni, G. Matteucci, G. Pozzi, and M. Vanzi, Phys. Rev. Lett. **55**, 2196 (1985).
30. B.G. Frost, L.F. Allard, E. Völkl and D.C. Joy (1995), Holography of electrostatic fields, In: A. Tonomura, L.F. Allard, G. Pozzi, D.C. Joy, and Y.A. Ono (eds.) Electron Holography. Elsevier, Amsterdam, pp. 169–179.
31. M.R. McCartney, D.J. Smith, R. Hull, J.C. Bean, E. Voelkl, and B. Frost, Appl. Phys. Lett. **65**, 2603 (1994).
32. W.D. Rau, P. Schwander, F.H. Baumann, W. Höppner and A. Ourmazd, Phys. Rev. Lett. **82**, 2614 (1999).
33. M.A. Gribelyuk, M.R. McCartney, J. Li, C.S. Murthy, P. Ronsheim, B. Doris, J.S. McMurray, S. Hedge, and D.J. Smith, Phys. Rev. Lett. **89**, 022502 (2002).
34. V. Ravikumar, R.P. Rodrigues, and V.P. Dravid, Phys. Rev. Lett. **75**, 4063 (1995).
35. J.S. Barnard and D. Cherns, J. Electron Microscopy **49**, 281 (2000).
36. M.R. McCartney, F.A. Ponce, J. Cai, and D.P. Bour, Appl. Phys. Lett. **76**, 3055 (2001).
37. A. Tonomura, N. Osakabe, T. Matsuda, T. Kawasaki, J. Endo, S. Yano, and H. Yamada, Phys. Rev. Lett. **56**, 792 (1986).
38. J. Bonevich, K. Harada, T. Matsuda, H. Kasai, T. Yoshida, G. Pozzi, and A. Tonomura, Phys. Rev. Lett. **70**, 2952 (1993).
39. N. Osakabe, K. Yoshida, S. Horiuchi, T. Matsuda, H. Tanabe, T. Okuwaki, J. Endo, H. Fujiwara, and A. Tonomura, Appl. Phys. Lett. **42**, 792 (1983).
40. R.F.C. Farrow, D. Weller, R.F. Marks, M.F. Toney, A. Cebollada, and G.R. Harp, J. Appl. Phys. **79**, 5330 (1996).
41. D.G. Streblechenko, M.R. Scheinfein, M. Mankos, and K. Babcock, IEEE Trans. Magn. **32**, 4124 (1996).
42. D.G. Streblechenko, Ph.D. dissertation, Arizona State University (1999).
43. G. Matteucci, G. Missiroli, E. Nichelatti, A. Migliori, M. Vanzi, and G. Pozzi, J. Appl. Phys. **69**, 1853 (1991).
44. G. Lai, T. Hirayama, A. Fukuhara, K. Ishizuka, T. Tanji, and A. Tonomura, J. Appl. Phys. **75**, 4593 (1994).
45. M.R. McCartney and Y. Zhu, Appl. Phys. Lett. **72**, 1380 (1998).
46. M.R. McCartney and Y. Zhu, J. Appl. Phys. **83**, 6414 (1998).
47. Y. Zhu and M.R. McCartney, J. Appl. Phys. 84, 3267 (1998).
48. H. Kronmüller (1990) In: Science and Technology of Nanostructured Materials, G.C. Hadjipanayis and G. Prinz (eds.). Plenum Press, New York. p. 657.
49. J.F. Herbst and J.J. Croat, J. Magn. Magn. Mater. **100**, 57 (1991).
50. B.O. Cullity (1992) Introduction to Magnetic Materials. Addison-Wesley, New York.
51. T. Hirayama, J. Chen, T. Tanji, and A. Tonomura, Ultramicroscopy **54**, 9 (1994).
52. R.E. Dunin-Borkowski, M.R. McCartney, D.J. Smith, and S.S.P. Parkin, Ultramicroscopy **74**, 61 (1998).
53. M. Mankos, J.M. Cowley, and M.R. Scheinfein, Phys. Stat. Sol. (a) **154**, 469 (1996).

54. M. de Graef, T. Nuhfer, and M.R. McCartney, J. Microscopy **194**, 84 (1999).
55. R.E. Dunin-Borkowski, M.R. McCartney, R.B. Frankel, D.A. Bazylinski, M. Posfai, and P.R. Buseck, Science **282**, 1868 (1998).
56. R.E. Dunin-Borkowski, M.R. McCartney, M. Posfai, R.B. Frankel, D.A. Bazylinski, and P.R. Buseck, Eur. J. Mineral. **13**, 671 (2001).
57. M.R. McCartney, U. Lins, M. Farina, P.R. Buseck, and R.B. Frankel, Eur. J. Mineral **13**, 685 (2001).
58. K.A. Fabian, A. Kirchner, W. Williams, F. Heider, T. Leibel, and A. Hubert, Geophys. J. Int. **124**, 89 (1996).
59. R.E. Dunin-Borkowski, M.R. McCartney, B. Kardynal, and D.J. Smith, J. Appl. Phys. **84**, 374 (1998).
60. R.E. Dunin-Borkowski, M.R. McCartney, B. Kardynal, D.J. Smith, and M.R. Scheinfein, Appl. Phys. Lett. **75**, 2641 (1999).
61. R.E. Dunin-Borkowski, M.R. McCartney, B. Kardynal , S.S.P. Parkin, M.R. Scheinfein, and D.J. Smith, J. Microscopy **200**, 187 (2000).
62. R.E. Dunin-Borkowski, M.R. McCartney, B. Kardynal, M.R. Scheinfein, D.J. Smith, and S.S.P. Parkin, J. Appl. Phys. **90**, 2899 (2001).
63. D.J. Smith, R.E. Dunin-Borkowski, M.R. McCartney, B. Kardynal, and M.R. Scheinfein, J. Appl. Phys. **87**, 7400 (2000).
64. M. Rührig, B. Khamsehpour, K.J. Kirk, J.N. Chapman, P. Aitchison, S. McVitie, and C.D.W. Wilkinson, IEEE Trans. Magn. 32, 4452 (1996).
65. J.C.S. Kools, IEEE Trans. Magn. **32**, 3165 (1996).
66. J. Bonevich, G. Pozzi, and A. Tonomura (1999) Electron holography of electromagnetic fields In: Introduction to Electron Holography, E. Völkl, L.F. Allard, and D.C. Joy (eds.). Kluwer Academic, New York. pp. 153–181.
67. J. Chen, T. Hirayama, G. Lai, T. Tanji, K. Ishizuka, and A. Tonomura, Opt. Rev. **2**, 304 (1994).